small methods
www.small-methods.com

Low-Cost, Scalable Fabrication of Multi-Dimensional Perovskite Solar Cells and Modules Assisted by Mechanical Scribing

*Hock Beng Lee, Asmaa Mohamed, Neetesh Kumar, Nurfatin Hafizah Zain Karimy, Vinayak Vitthal Satale, Barkha Tyagi, Do-Hyung Kim, and Jae-Wook Kang**

The performance and scalability of perovskite solar cells (PSCs) based on 3D formamidinium lead triiodide ($FAPbI_3$) absorber are often hindered by defects at the surface and grain boundaries of the perovskite. To address this, the study demonstrates the use of pyrrolidinium iodide for the in situ formation of an energetically aligned 1D pyrrolidinium lead triiodide ($PyPbI_3$) capping layer over the 3D $FAbI_3$ perovskite. The thermodynamically stable $PyPbI_3$ perovskitoids, formed through cation exchange reactions, effectively reduce surface and grain boundary defects in the $FAPbI_3$ perovskite. In addition to improved phase stability, the resulting 1D/3D perovskite film forms a cascade energy band alignment with the other functional layers in PSCs, enabling a barrier-free interfacial charge transport. With a maximum power conversion efficiency (PCE) of ≈23.1% and ≈20.7% at active areas of 0.09 and 1.05 cm^2, respectively, the 1D/3D PSCs demonstrate excellent performance and scalability. Leveraging this improved scalability, the study has successfully developed a mechanically-scribed 1D/3D perovskite mini-module with an unprecedentedly high PCE of ≈20.6% and a total power output of ≈270 mW at an active area of ≈13.0 cm^2. The 1D/3D multi-dimensional perovskite film developed herein holds great promise for producing low-cost, high-performance perovskite photovoltaics at both the cell and module levels.

1. Introduction

Solution-processed, lab-scale perovskite solar cells (PSCs) based on archetypal three-dimensional (3D) perovskite films have an astounding power conversion efficiency (PCE) of >25% which surpasses the performance benchmark of the photovoltaic industry.[1] Despite its excellent single-cell efficiency, the full commercialization of PSCs remains a steep challenge because the defect-prone 3D perovskite absorber film lacks the environmental stability and scalability to produce large-area power modules as efficiently as conventional silicon wafer-based solar cells. Currently, formamidinium lead triiodide ($FAPbI_3$) is the most scrutinized 3D perovskite absorber for lab-scale PSCs because it exhibits many interesting features, such as a narrow optical bandgap (E_g), long carrier-diffusion lengths, high absorption coefficient, and a near-optimal Goldschmidt tolerance factor.[2] However, 3D $FAPbI_3$ perovskite has a polymorphic nature, in which the metastable black α-$FAPbI_3$ tends to transform into yellow δ-$FAPbI_3$ with a wide-bandgap upon prolonged exposure to high temperature and moisture.[3] The crystal polymorphic behavior of $FAPbI_3$ perovskite can be linked to involuntary migrations of formamidinium/methylammonium/cesium/-constituents embedded in the center of corner-sharing metal-halide $[PbI_6]^{4-}$ octahedra in the 3D framework.[4] In the pristine

H. B. Lee, A. Mohamed, N. H. Zain Karimy, V. V. Satale, J.-W. Kang
Department of Flexible and Printable Electronics
LANL-JBNU Engineering Institute-Korea
Jeonbuk National University
Jeonju 54896, Republic of Korea
E-mail: jwkang@jbnu.ac.kr

The ORCID identification number(s) for the author(s) of this article can be found under https://doi.org/10.1002/smtd.202400850

DOI: 10.1002/smtd.202400850

A. Mohamed
Department of Physics
Faculty of Science
South Valley University
Qena 83523, Egypt

N. Kumar
Department of Mechanical and Materials Engineering
Florida International University
Miami, FL 33174, USA

B. Tyagi
Department of Physics
University of Oxford
Oxford OX1 3PU, UK

D.-H. Kim
KEPCO Research Institute
Korea Electric Power Corporation
105 Munji-Ro, Yusung-Gu, Daejeon 34056, Republic of Korea

state, the surface of the $FAPbI_3$ perovskite accommodates a substantial number of native point defects, particularly iodide vacancies, pinholes, and grain boundaries that cause carrier recombination and allow oxygen and moisture permeation.[5] These imperfections are the culprits behind the poor stability and scalability of the perovskite film.

Conceptually, 3D perovskites are preferred for photovoltaic applications because they exhibit a high dielectric constant and an interconnected 3D lattice framework that allows spontaneous charge separation and multi-directional charge transport. However, the abundant point defects and inadequate electrostatic interactions between the organic and inorganic elements in the 3D lattice network can trigger involuntary halide ion migrations, rendering the 3D perovskite highly susceptible to environmental degradation.[6] Strategies such as additive engineering,[7,8] antisolvent engineering,[9] surface passivation and functionalization,[10] interfacial modification,[11] vapor treatment,[12] and low-dimensional perovskite modification[13] have been adopted to control the defects and enhance the stability as well as scalability of the 3D perovskite. Among these strategies, tailoring the dimensionality and crystal phase of 3D perovskite through the use of bulky organic spacer cation is considered the most effective approach to quench the native defects and inhibit phase degradation. There has been a growing focus on using 2D or quasi-2D perovskites, composed of atomically thin perovskite slabs as moisture barriers, to enhance the stability of PSCs. Although 2D or quasi-2D perovskites are more thermodynamically stable than the 3D perovskites, the van der Waals gap arising from the use of insulating organic spacers can form multiple-quantum-well electronic band structures that induce internal quantum confinement effect and the enlargement of E_g.[14] Moreover, the disparity in the dielectric constant between the alternating perovskite slabs and the organic spacer layers in the quasi-2D structures can also lead to the energy barrier and dielectric confinement effect that affect charge transport dynamics.[15,16]

Researchers have recently been exploring the modification of 3D perovskites using low-dimensional perovskitoids (LDP), known for their flexible $[PbI_6]^{4-}$ octahedra connection styles, self-healing characteristics, and high thermodynamic and moisture stability.[17] Unlike the proper corner-sharing $[PbI_6]^{4-}$ octahedra architecture in 3D perovskite, the $[PbI_6]^{4-}$ octahedra in LDP structures can be linked by edge-sharing, face-sharing, corner-sharing, or combinations of all of these to form a 1D lattice configuration.[18] LDP can be formed with the use of appropriate organic spacers, either by incorporating them as an additive in the precursor stage or by depositing them over the perovskite layer post-preparation. For instance, Gao et al. and Chen et al. utilized thiazole ammonium (TA) and 1,10-phenanthroline (Phen) cations to form $(TAPbI_3)$ and PbI_2(Phen) 1D-structured perovskite capping layer over 3D perovskite, respectively.[19,20] Pham's and Xe's groups employed pyrrolidinium cation (Py^+) to form molecular 1D pyrrolidinium lead iodide ($PyPbI_3$), producing a thermodynamically stable 1D/3D perovskite heterostructure.[21,22] In these studies, the efficiency and stability of the PSCs improved tremendously in the presence of a 1D perovskite capping layer that functioned as an effective moisture barrier. Despite the technological advancement of 1D/3D PSCs, the formation mechanism of LDP nanostructures is scarcely discussed and correlated to the device performance and scalability of PSCs.

The optoelectronic properties, band structure, and stability of LDP are highly dependent on the size and molecular structure of the spacer cations used. Most of the spacer cations exhibit long alkyl chains that can create hindrance to charge transport when not properly controlled. In this study, we showcase the use of relatively smaller pyrrolidinium iodide (PyI) molecules for the in situ formation of a lattice-matched 1D $PyPbI_3$ capping layer on top of the 3D $FAPbI_3$ perovskite film. The molecular structure of PyI contains an amino group ($-NH_2$) that can spontaneously interact with the undercoordinated Pb^{2+} ions on the surface of 3D perovskite, forming either a coordinate or dative-covalent bond.[23,24] Additionally, the free Py^+ provided by the PyI molecules can undergo cation exchange reactions with the native formamidinium cation (FA^+) in the 3D perovskite lattice to form $PyPbI_3$ perovskitoids, resulting in a unique 1D/3D perovskite heterostructure with a favorable energy landscape for PSC application. Our experimental findings indicate that the 1D/3D perovskite film produced through PyI passivation exhibited significantly fewer morphological defects and was able to form a cascade energy band structure with the other functional layers in PSCs. The molecular 1D $PyPbI_3$ perovskitoids primarily settle at surface grain boundaries, thereby kinetically suppressing the $\alpha \rightarrow \delta$ phase transition in the 3D perovskite. Due to barrier-free interfacial charge transfer, reduced trap-assisted carrier recombination, and lower V_{oc} deficit, the top-performing 1D/3D PSC achieved a maximum PCE of 23.1%, marking one of the best performances to date for 1D/3D PSCs. Moreover, the 1D/3D PSC displayed improved environmental stability, attributed to the presence of a thermodynamically stable $PyPbI_3$ capping layer that impedes O_2 and moisture permeation. The scalability of 1D/3D PSCs is outstanding, demonstrating ≈90% PCE retention as the device active area is increased from 0.09 cm^2 to 1.05 cm^2. Leveraging this scalability, we were able to scale up the PSC device fabrication from a single cell to a module. To create an effective module circuit design, a laser scriber is typically required to selectively etch the functional layers and top/bottom contact of the PSCs with precise control. However, many research groups encounter challenges in producing high-performance perovskite modules because laser scriber instruments are not widely accessible. To overcome this limitation, this study aims to propose the use of mechanical scribing methods as a low-cost alternative for fabricating perovskite modules with competitive performance in instances where a laser scriber is not available. By employing the mechanical scribing approach and 1D/3D perovskite absorber film, the best mechanical-scribed 1D/3D PSC module achieved an impressive module efficiency of ≈20.6%, with a total power output of ≈270 mW over an active area of ≈13.0 cm^2. This result highlights the benefits of the mechanical scribing method from a cost perspective. The significantly enhanced performance of the 1D/3D perovskite solar device at both the cell and module levels confirms that dimensionality engineering is pivotal for the future development and commercialization of low-cost, large-area perovskite photovoltaics.

2. Results and Discussion

The 3D $FAPbI_3$-based triple-cation perovskite films were prepared using pre-synthesized high-purity δ-$FAPbI_3$ perovskite

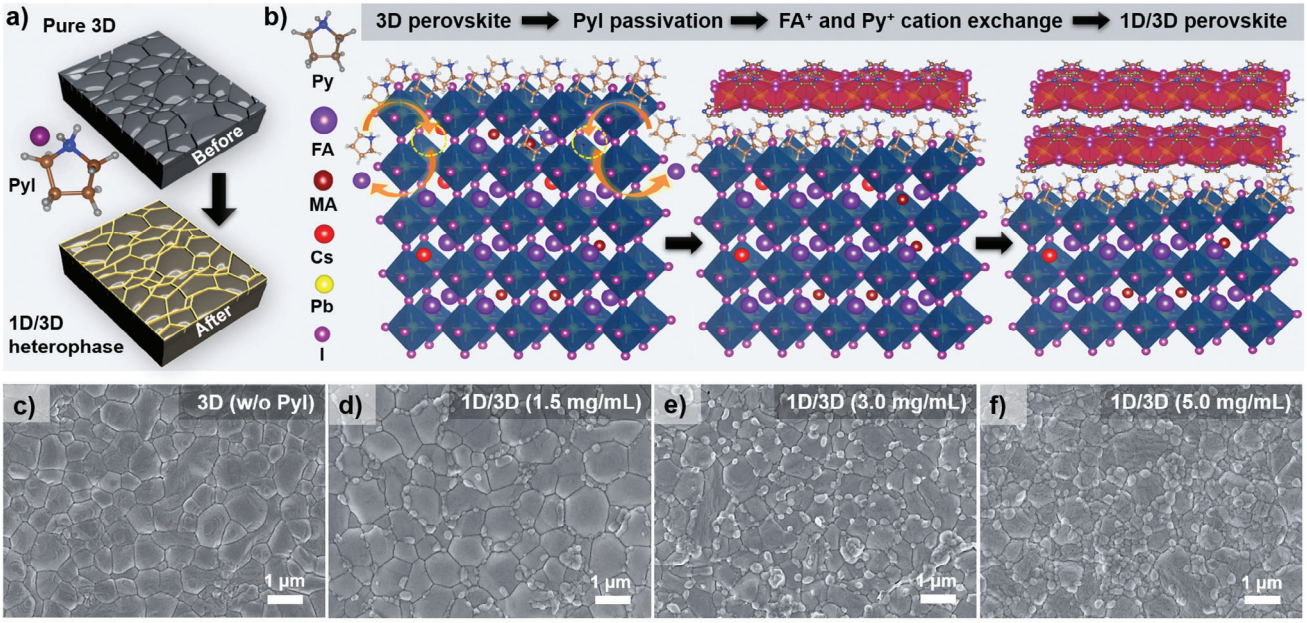

Figure 1. a) Schematic fabrication process of 1D/3D perovskite film through extrinsic PyI passivation strategy. b) Structural transition of the perovskite lattice from pristine 3D structure into 1D/3D heterostructure via cation-exchange reactions. High-resolution FESEM images of c) pristine 3D, d) 1D/3D (1.5 mg mL^{-1} PyI), e) 1D/3D (3.0 mg mL^{-1} PyI), and f) 1D/3D (5.0 mg mL^{-1} PyI) perovskite films.

powder through a one-step mixed antisolvent technique, as demonstrated in our previous work.[9] In its pristine state, 3D polycrystalline perovskite film contains a high number of defects on its surface, such as grain boundaries, uncoordinated atoms, interstitial defects, dangling bonds, and chemical impurities. The density of surface defects in a 3D perovskite film is estimated to be several magnitudes higher than that in the bulk,[5] and the defects can create deep-level traps that significantly hinder the charge transport of PSCs. To address this issue, we used pyrrolidinium iodide (PyI) as a bifunctional organic spacer and defect passivator to create a low-dimensional perovskite capping layer that alleviates the surface imperfections of 3D perovskite film. Pyrrolidinium cations (Py^+) are relatively small in size compared to the other bulky organic spacer cations and they can penetrate into the lattice of 3D $FAPbI_3$ during the surface passivation process. During the incorporation process, the Py^+ are arranged in a hexagonal manner between the two 1D face-sharing $[PbI_3]^-$ octahedra chains, enabling the in situ formation of 1D $PyPbI_3$ perovskitoids on the surface of 3D $FAPbI_3$ lattice (**Figure 1a**).

1D $PyPbI_3$ perovskitoids are thermodynamically stable and exhibit a lattice-matching crystal configuration with the underlying 3D $FAPbI_3$ perovskite, therefore can lead to the formation of 1D/3D multi-dimensional perovskite film without creating additional electrical transport barrier. This unique 1D/3D perovskite heterophases can be formed in two ways: i) by adding PyI as an additive during the precursor stage or ii) by applying PyI on the perovskite film after deposition to act as a surface passivator. Although both methods can produce multi-dimensional perovskite films with a 1D/3D heterostructure, it is easier to control the distribution of the $PyPbI_3$ LDPs in the 3D perovskite film using the post-deposition method. In the post-deposition method, the bulky PyI molecules are expected to stay on the 3D perovskite surface and interact with the undercoordinated surface Pb atoms. The modification process starts with Py^+ ions being adsorbed on the perovskite surface, which then undergoes cation exchange reactions with the native FA^+ ions and negatively charged defects in the lattice vacancies through electrostatic interactions.[25] This triggers the formation of $PyPbI_3$ perovskitoids through a 3D → 1D molecular reorganization process, as expressed in the Equation (1) below:

$$FAPbI_3\,(s) + PyI\,(sol) = PyPbI_3\,(s) + FA\,(g) \quad (1)$$

During the dynamic spin-coating process, the voluntary exchange of FA ↔ Py cations can lead to the (i) dissolution of $FAPbI_3$ lattice due to the escape of FA^+ ions in the form of formamidine (FA) gas and (ii) recrystallization into a 1D $PyPbI_3$ lattice in the presence of absorbed Py^+ ions (Figure 1b). Simultaneously, the free I^- ions from the PyI molecules can occupy the halide vacancies in the lattice network of $FAPbI_3$ and perform defect passivation.[25] With an increase in PyI passivation concentration, the $FAPbI_3$ perovskite will be exposed to more adsorbed Py^+ ions, allowing more cation exchange between Py^+ and FA^+ ions. This phenomenon further accelerates the dissolution of $FAPbI_3$ perovskite and the recrystallization of the $PyPbI_3$ perovskite. Thus, the 1D phase in the PyI-modified perovskite film becomes increasingly dominant with increasing PyI concentration. It should be noted that the generation of 1D $PyPbI_3$ lattice occurs predominantly on the surface of the bulk perovskite film because Py^+ are larger in size compared to the native A-site cations of $FAPbI_3$ such as FA^+, methylammonium (FA^+) and cesium (Cs^+) cations. Nonetheless, the presence of the 1D $PyPbI_3$ capping layer can reduce the formation energy difference between the δ and α phase of the underlying 3D perovskite, thus inhibiting the phase transition in 1D/3D multi-dimensional perovskite to achieve better stability.

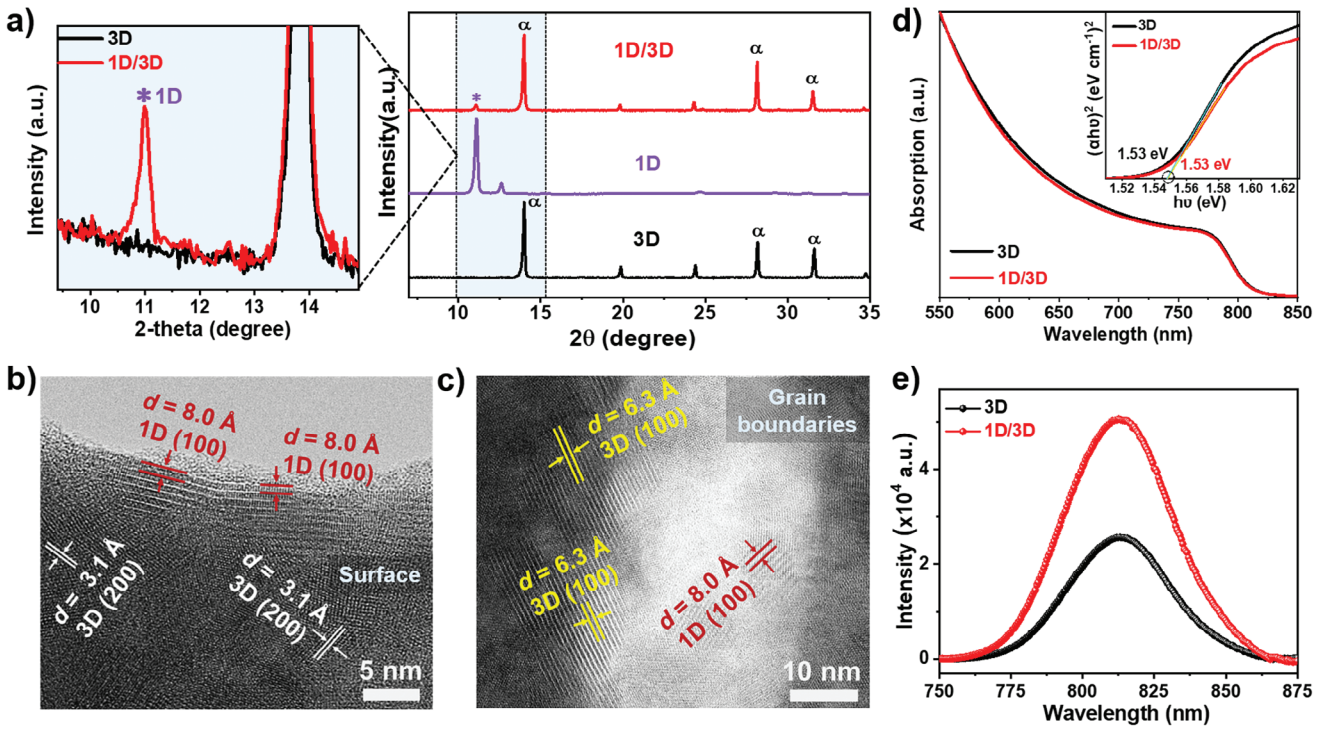

Figure 2. a) XRD patterns showing the crystallography of pristine 3D (triple-cation) perovskite, 1D ($PyPbI_3$) perovskite, and 1D/3D heterostructure perovskite samples. b). High-resolution TEM images of PyI-modified perovskite sample captured on (b) the uppermost surface region and c) grain boundary region. Optical properties: d) absorption spectra and Tauc plots (inset), and e) PL spectra of pristine 3D and 1D/3D perovskite films.

The molecular interactions between the Py^+ cations and the inorganic $[PbI_3]^-$ chains in $FAPbI_3$ were examined using attenuated total-reflectance Fourier transform infrared (ATR-FTIR) spectroscopy. Figure S1 (Supporting Information) displays the ATR-FTIR spectra of the pure FAI, pure PyI, and $FAPbI_3$ films passivated with varying concentrations of PyI. The neat FAI displays broadened transmissions from ν(N-H) at ≈3380 cm^{-1} and ν(C═N) at ≈1720 cm^{-1}. Meanwhile, the neat PyI exhibits two broadened transmissions from ν(N-H) at ≈3450 cm^{-1} and ν(C-H) at ≈2989 cm^{-1}. Upon closer examination, it was observed that there is a strong molecular interaction between FA^+ and $[PbI_3]^-$ moieties present in all perovskite films, leading to the narrowing and splitting of the ν(N-H) into quadruple bands at 3400, 3355, 3331, and 3269 cm^{-1}. The vibrational bands of PyI ultimately merged with the ν(N-H) quadruple band of the PyI-passivated $FAPbI_3$ films, suggesting strong coordination of Py^+ with the $[PbI_3]^-$ moieties of $FAPbI_3$. No traces of unreacted Py^+ were observed in the passivated perovskite films, as evidenced by the disappearance of the signature ν(N-H) of PyI, confirming that all Py^+ completely transformed into $PyPbI_3$.

The field-emission scanning electron microscope (FESEM) top-view images in Figure 1c–f depict the surface morphologies of the perovskite film treated with various concentrations of PyI (1.5, 3.0, and 5.0 mg mL^{-1}). Before PyI passivation, distinct hexagonal perovskite grains were visible on the surface of the pristine 3D perovskite film. (Figure 1c). Interestingly, PyI passivation has led to the scattered growth of LDP nanostructures, particularly along the grain boundaries. These loosely-packed LDP nanostructures are more thermodynamically stable and less susceptible to environmental degradation, which can prevent the $\alpha \rightarrow \delta$ phase transformation in 3D perovskite. An increase in the concentration of PyI passivation further accelerated the growth of LDP nanostructures near the grain surface and boundary regions, giving rise to 1D/3D heterostructure perovskite film. In addition to growing 1D $PyPbI_3$, the PyI molecule acted as a defect mediator, passivating the surface grain boundaries that accommodate abundant native defects (charge trap sites) in the perovskite film. Grain size analysis results (histogram plots) showed that the pristine 3D and 1D/3D perovskite films had average grain sizes of ≈702 and ≈733 nm, respectively (Figure S2, Supporting Information).

X-ray diffractometer (XRD) analysis was performed to study the structural properties and crystallography of the 3D $FAPbI_3$ perovskite, 1D $PyPbI_3$ perovskite, and 1D/3D multi-dimensional perovskite samples. As observed in **Figure 2a**, the pristine 3D perovskite film exhibited dominant (100) and (200) diffraction peaks corresponding to a cubic α-$FAPbI_3$ structure (space group $Pm\bar{3}m$, a = 6.3621 Å),[3] featuring a 3D network with corner-sharing $[PbI_6]^{4-}$ octahedra.[9] After PyI passivation, the 1D/3D (PyI-modified) perovskite films also displayed a cubic 3D-perovskite structure with a preferred orientation along the (100) and (200) crystal facets. With an increase in PyI concentration up to 5.0 mg mL^{-1}, the crystallinity of the perovskite film was gradually enhanced (Figure S3a, Supporting Information). Interestingly, the high-resolution XRD pattern (inset of Figure 2a) revealed the presence of a subtle (*-denoted) diffraction peak at a 2θ of ≈10.9° in the 1D/3D perovskite film (Figure S3b, Supporting Information). This peak suggests the possible

formation of 1D $PyPbI_3$ on the 3D perovskite, as it does not match with the crystallography of pure PyI salt. To confirm the origin of this subtle peak, we synthesized phase-pure 1D $PyPbI_3$ perovskite using an antisolvent-assisted crystallization method and investigated its crystallography. The XRD pattern of $PyPbI_3$ perovskite exhibits a dominant diffraction peak (2θ of ≈10.9°) corresponding to (100) plane reflections of the hexagonal crystal structure (space group $P6_3/mmc$, $a = 9.3117$ Å) of $PyPbI_3$ with a 1D $[PbI_3]^-$ chain network.[26] In the analysis of crystallography, the asterisk (*) marked peak in the PyI-modified sample can be attributed to the presence of $PyPbI_3$, confirming the role of PyI as an organic passivator in forming a 1D/3D multi-dimensional perovskite film. Since no diffraction peak corresponding to PyI crystal was detected, it can be assumed that all PyI salts were involved in cation exchange reactions and fully converted into $PyPbI_3$. The formation of the 1D $PyPbI_3$ phase on the 3D perovskite surface was enhanced with the increase in PyI passivation concentration due to the intensified $Py^+ \leftrightarrow FA^+$ cation exchange reactions, as reflected by the higher intensity of the (100) peak for 1D $PyPbI_3$ (Figure 2a). Literature suggests that the lattice mismatch arising from the coexistence of different dimensionality and crystal phases, such as the 1D $PyPbI_3$ (orthorhombic) 3D $FAPbI_3$ (cubic) herein, can result in a strained polycrystalline crystal structure with poor structural stability and interfacial discontinuity.[5] To investigate this, the lattice strains of the pristine 3D and 1D/3D perovskite films were characterized by XRD, and the strain was computed using the Williamson-Hall method. Interestingly, the results (Figure S3c, Supporting Information) show that the strain due to lattice mismatch decreased by ≈35% for 1D/3D perovskite film (1.5 mg mL^{-1} PyI) compared to the 3D perovskite film. This phenomenon is attributed to the Vander Waals and hydrogen bonds between $PyPbI_3$ and $FAPbI_3$ perovskites, which allows epitaxial growth of incoherent in-plane lattice at the 1D/3D heterojunction interfaces, facilitating the bond-free integration of 1D and 3D perovskite structures while minimizing the strain from lattice mismatch.[5,27] This finding is consistent with density-functional theory (DFT) simulation results reported in the work of Cha et al., demonstrating the thermodynamically favorable formation of 1D $PyPbI_3$ system (based on pyridine bromide) on the surface of 3D $FAPbI_3$ system with lattice-matched 1D/3D heterojunctions.[18] The mitigated lattice-mismatch at 1D/3D heterojunctions following PyI passivation is highly beneficial to the structural stability and optoelectronic properties of the 1D/3D perovskite film. Additionally, there are no discernible differences in the crystallography of the 1D/3D perovskite film after high-temperature (150 °C) annealing (Figure S3d, Supporting Information).

The 1D/3D (PyI-modified) perovskite film was analyzed using focused-ion-beam transmission electron microscopy (FIB-TEM) to confirm the coexistence of 1D and 3D perovskite phases. The resulting FIB-TEM images in Figure S4 (Supporting Information) show the layer-by-layer stacked configuration (ITO/SnO_2/perovskite/carbon) of the scanned sample. Different areas on the perovskite film surface were imaged using FIB-TEM, and the distinct lattice fringes in the images allowed the identification of the 1D and 3D perovskite phases. In the uppermost region of the perovskite surface (sample/carbon interface) where $PyPbI_3$ LDPs were predominantly present, visible lattice fringes (marked in red) with an interplane distance (d-spacing) value of 8.0 Å can be observed (Figure 2b). These lattice fringes can be indexed to the (110) diffraction plane of the 1D orthorhombic $PyPbI_3$ crystal, confirming the growth of 1D crystal phase in the perovskite film after PyI passivation. Deeper into the film surface, lattice fringes marked in white with interplane distances or d-spacing of 3.10 Å corresponding to (200) planes of the 3D cubic $FAPbI_3$ crystal were also detected. In addition, both 1D and 3D perovskite phases were detected near the surface grain boundary region, as shown in Figure 2c. Similarly, the visibly larger lattice fringes marked in red with a d-spacing of 8.0 Å are associated with the (100) planes of 1D $PyPbI_3$ crystal, while the smaller lattice fringes marked in yellow with an interplane distance of 6.3 Å are related to the (100) diffraction plane of the 3D cubic $FAPbI_3$ crystal. The 1D and 3D phases were intricately linked within the perovskite lattice, suggesting that the overlaying 1D $PyPbI_3$ capping layer has a lattice-matching crystal configuration with the underlying 3D $FAPbI_3$ perovskite. The ability of 1D $PyPbI_3$ to integrate with the 3D $FAPbI_3$ lattice along various crystal planes has resulted in a 1D/3D multi-dimensionality in the PyI-modified perovskite film without creating significant lattice strain or charge transport barrier. The selected-area electron diffraction pattern in Figure S5 (Supporting Information) reveals the polycrystalline nature of the perovskite layer in the film.

Figure 2d shows that the optical properties of the pristine 3D and 1D/3D perovskite films are somewhat similar, indicating that the presence of 1D $PyPbI_3$ capping layer did not impact the absorption edge position of the 3D perovskite. The Tauc plot (inset) reveals that the 1D/3D perovskite film has a comparable optical bandgap (E_g) of 1.53 eV to that of the 3D perovskite film. The optical absorption spectra of perovskite films treated with different concentrations of PyI are provided in Figure S6 (Supporting Information). Concurrently, the steady-state PL spectra (Figure 2e) demonstrate that the 1D/3D perovskite film exhibited a higher radiative PL emission compared to the pristine 3D counterpart, which can be attributed to the passivation of defect-induced trap states by the $PyPbI_3$ capping layer.[28]

The surface chemical compositions of the pristine 3D and 1D/3D (PyI-modified) perovskite films were investigated via XPS measurements. The XPS survey scan spectra (Figure S7, Supporting Information) and core-level spectra (Figures S8 and S9, Supporting Information) revealed that both 3D and 1D/3D perovskite samples mainly consisted of cesium (Cs), lead (Pb), iodide (I), bromide (Br), and nitrogen (N), and carbon (C) elements, which are the primary constituents of the 3D triple-cation perovskite. While oxygen (O) is not the primary constituent element of perovskite film, it was detected in both samples, and its presence offers valuable insight into the surface composition of the perovskite film. To provide a more concise analysis, the spectra of the mentioned elements were deconvoluted. In **Figure 3a**, the broad O 1s spectra of both perovskite samples can be deconvoluted into three subpeaks with different binding energies (B.E.), namely O_1 (B.E ≈531.6 eV), O_2 (B.E ≈532.4 eV), and O_3 (B.E ≈533.6 eV). These O components mainly originated from the degradation of perovskite film due to exposure to surrounding air (O_2) and humidity (H_2O), as explained by Correa-Baena's group.[6] The O_1 peak could be attributed to the formation of carbonates (CO_3^{2-}) in the perovskite film resulting from exposure to H_2O/air, such as $PbCO_3$. Meanwhile, the O_2 peak and

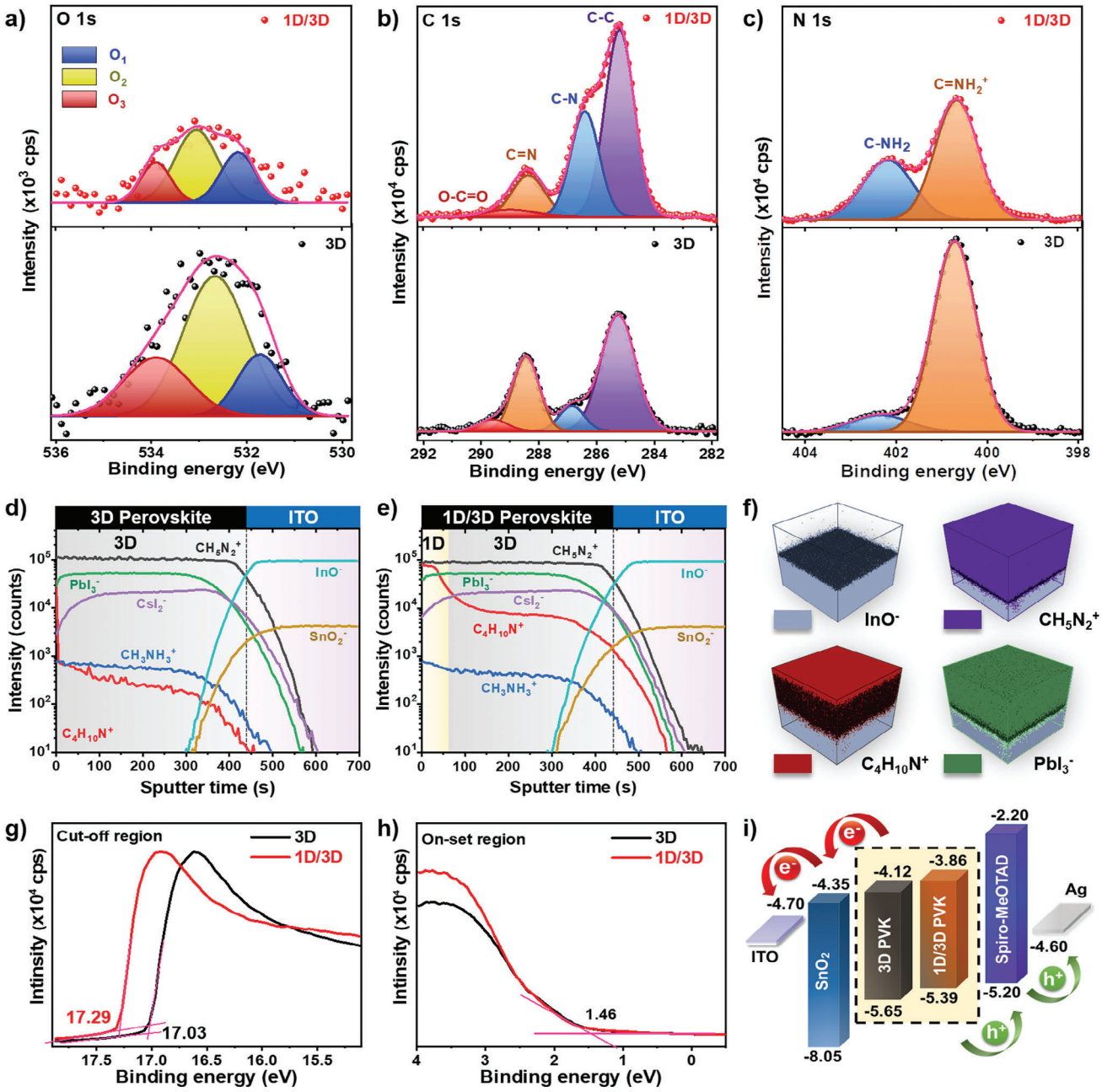

Figure 3. XPS surface composition analysis: a) O1s, b) C 1s, and c) N 1s core-level spectra of pristine 3D and 1D/3D perovskite samples. ToF-SIMS depth profiles of the d) pristine 3D and e) 1D/3D perovskite films deposited on ITO substrate. f) Corresponding ToF-SIMS 3D tomography of the 1D/3D perovskite samples. UPS spectra displaying the g) secondary electron cutoff region and h) valence band onset region of 3D and 1D/3D perovskite samples. i) Schematic figure illustrating the band offsets between 3D and 1D/3D perovskite films with the other functional layers in a PSC device.

O_3 peak suggest the presence of adsorbed O_2 molecules (O_{ads}) and dangling hydroxyl groups (–OH) on the perovskite surface, respectively. Literature also associates the O_3 peak with $Pb(OH)_2$ formation due to moisture permeation.[29] Table S1 (Supporting Information) summarizes the precise atomic percentages of these O components. The 1D/3D perovskite sample exhibited a significantly lower O atomic ratio than the 1D/3D perovskite sample, indicating the reduction of non-perovskite phases such as $PbCO_3$ and $Pb(OH)_2$, and O-related defects such as O_{ads} and -OH on its surface. The lower O 1s atomic ratio in the 1D/3D perovskite film compared to the pristine counterpart evidenced that the $PyPbI_3$ capping layer effectively shielded the perovskite from H_2O/air permeation.

The Pb 4f core-level spectra of both the 3D perovskite and 1D/3D perovskite samples displayed two Pb $4f_{7/2}$ and Pb $4f_{5/2}$ peaks at B.E. of ≈138.6 eV and ≈143.4 eV, respectively (Figures S8 and S9, Supporting Information). These peaks originated from the primary Pb constituents in the perovskite lattice. There

were minimal traces of metallic Pb atoms (Pb_0) in both 3D and 1D/3D films, indicating a very low amount of unreacted Pb in the perovskite film.[30] Meanwhile, both I 3d spectra of the 3D and 1D/3D perovskite samples displayed two primary peaks corresponding to I $3d_{3/2}$ and I $3d_{5/2}$ spin orbits. According to the area under the curve calculation (Table S2, Supporting Information), the I/Pb ratio in 1D/3D perovskite film is higher, which is attributable to the additional iodine content supplied by the PyI passivator molecules during surface passivation treatment. A 3D perovskite film typically contains a high density of halide (iodine) vacancies due to the migration of halide (iodine)-neutral atoms within the adjacent lattice in its 3D network.[2,31] Thus, the additional I^- ions from the PyI passivators can occupy the pre-existing iodine vacancies in the 3D lattice network, thereby improving the stoichiometry of the perovskite film.

Figure 3b reveals significant differences between the C 1s core-level spectra of 3D and 1D/3D perovskite samples. The broad asymmetric C 1s core-level spectra of both samples were deconvoluted into a C-C peak (B.E. ≈285.0 eV), a C-N peak (B.E. ≈285.6 eV), a C = N peak (B.E. ≈288.4 eV) and O-C═O (B.E. ≈289.3 eV). In the 1D/3D perovskite sample, the C-C adventitious peak and C-N subpeak are relatively higher due to the molecular structure of PyI, which contains C-C and C-N molecular bonds. Conversely, there are reductions in the intensities of $C{=}NH_2$ and O-C═O peaks after PyI passivation. The C═N bond is associated with the native FA^+ ion in the perovskite lattice, whereas the O-C═O peak could originate from the $PbCO_3$ formed on the perovskite surface. The detection of the carbonate peak in the C 1s spectrum aligns well with the finding of $PbCO_3$ in the O 1s spectrum. The increased detection of the C-N bonds, coupled with the reduced intensity of the C = N bonds, implies that the perovskite film surface is dominated by Py^+ (from 1D $PyPbI_3$) instead of FA^+ (from 3D $FAPbI_3$) following PyI passivation. The N spectra were deconvoluted into two subpeaks corresponding to $C{=}NH_2{}^+$ (BE ≈400.7 eV) and $C\text{-}NH_2$ (BE ≈402.2 eV) bonds (Figure 3c). Similarly, the detection of the $C\text{-}NH_2$ peak, originating from Py^+, was higher in the 1D/3D perovskite sample, while the intensity of $C{=}NH_2$ peak originating from FA^+ was reduced. This finding correlates well with the C 1s spectra analysis, reflecting that PyI passivation has successfully induced the formation of $PyPbI_3$ via cation exchange reactions that result in the release of volatile FA from the perovskite network.

The vertical composition of the perovskite films was further analyzed using time-of-flight secondary ion mass spectrometry (ToF-SIMS) measurements. The resulting ToF-SIMS depth profiles in Figure 3d,e illustrate the vertical distribution of ions in the pristine 3D and 1D/3D perovskite films as a function of sputter time, respectively. Based on the ToF-SIMS profiles, the $PbI_3{}^-$, $CsI_2{}^-$, $CH_5N_2{}^+$ (corresponding to FA^+), and $CH_3NH_3{}^+$ (corresponding to MA^+) ions in the perovskite region, and InO^- and $SnO_2{}^-$ ions in the ITO region are homogeneously distributed. There is a signal of $C_4H_{10}N^+$ (corresponding to Py^+) in the 3D perovskite, which comes from background detection. As previously explained in the literature,[32] it is expected to observe characteristic ions such as $C_4H_{10}N^+$ even when their corresponding compound (in this case, Py^+) is absent due to the fragmentation of other molecular compounds (in this case, FA^+ and MA^+) during sputtering. However, the signal intensity of the $C_4H_{10}N^+$ increased by a few orders of magnitude in the 1D/3D perovskite sample when the corresponding compound (Py^+) was present. In the case of the 1D/3D perovskite sample, the signal of Py^+ is the strongest on the surface and reduced substantially with the increase of sputtered depth. This finding confirms that the Py^+ accumulates primarily at the surface or surface grain boundaries of the perovskite film to form $PyPbI_3$ capping layer that inhibits oxygen and moisture permeation. The interface transition region from the 1D perovskite to the 3D perovskite can be estimated by fitting the change in intensity of the Py^+ to the background (no Py^+). Correspondingly, the $C_4H_{10}N^+$ ions in the 1D/3D perovskite film had a stratified distribution compared to the $CH_5N_2{}^+$ and $PbI_3{}^-$ ions, as visualized in the ToF-SIMS 3D tomography (Figure 3f).

Simultaneously, UPS measurements were carried out to investigate the effect of PyI passivation on the work function and electronic band structure of the perovskite film. The E_{cutoff} and E_{onset} values of the pristine 3D and 1D/3D perovskite films were determined from the photoemission spectra in the secondary electron cutoff region (Figure 3g) and valence band onset region (Figure 3h), respectively. There was an upshift in the highest occupied molecular orbitals (HOMO) levels of perovskite film from −5.65 eV (3D perovskite) to −5.39 eV (1D/3D perovskite) after PyI modification, as calculated using Equation S1–S3. The lowest unoccupied molecular orbitals (LUMO) levels of the perovskite film also upshifted from −4.12 eV (3D perovskite) to −3.86 eV (1D/3D perovskite), while the E_g values for both perovskite films were the same (Table S3). Based on the obtained values, the energy band structures of 3D and 1D/3D perovskite films were illustrated in conjunction with the other functional layers (ITO, SnO_2 ETL, spiro-MeOTAD, and Ag) in a complete PSC device (Figure 3i). With PyI passivation, the HOMO level of 1D/3D perovskite sample exhibited a smaller energy band offset with the valence band of spiro-MeOTAD HTL, which could further facilitate the charge transport efficiency of PSCs.[23] The XPS and UPS results collectively prove that the 1D/3D perovskite film is more favorable for PSC application compared to the pristine 3D analog.

After investigated how PyI passivation affected the structural and optoelectronic properties of perovskite film, we proceeded to study the photovoltaic performance of PSCs based on pristine 3D and 1D/3D (PyI-modified) perovskite films. Prior to this, we assessed the device performance of 1D/3D PSCs treated with varying concentrations of PyI (0.5, 1, 1.5, 3.0, and 5.0 mg mL^{-1}). The results in Figures S10 and Table S4 (Supporting Information) indicate that the optimal PyI concentration for achieving the best performance in 1D/3D PSCs was 1.5 mg mL^{-1}. This concentration effectively passivated the surface imperfections of the perovskite film through the formation of $PyPbI_3$ LDPs. When the concentration of PyI was high (5.0 mg mL^{-1}), the performance of the 1D/3D PSCs deteriorated as the $PyPbI_3$ capping layer became excessively thick, hindering the perovskite-HTL interfacial charge transfer. Therefore, the concentration of PyI was fixed at 1.5 mg/mL for the fabrication of 1D/3D PSCs. For clarity, the PSC device based on pristine 3D and 1D/3D perovskite film will be denoted as 3D PSC and 1D/3D PSC, respectively, in the discussion henceforth.

As illustrated in the inset of **Figure 4a**, the planar PSCs had a conventional device architecture of ITO/SnO_2 bilayer/perovskite/spiro-MeOTAD/Ag. Our previous study demonstrated that the dopant-free SnO_2 bilayer (Bi-SnO_2) has

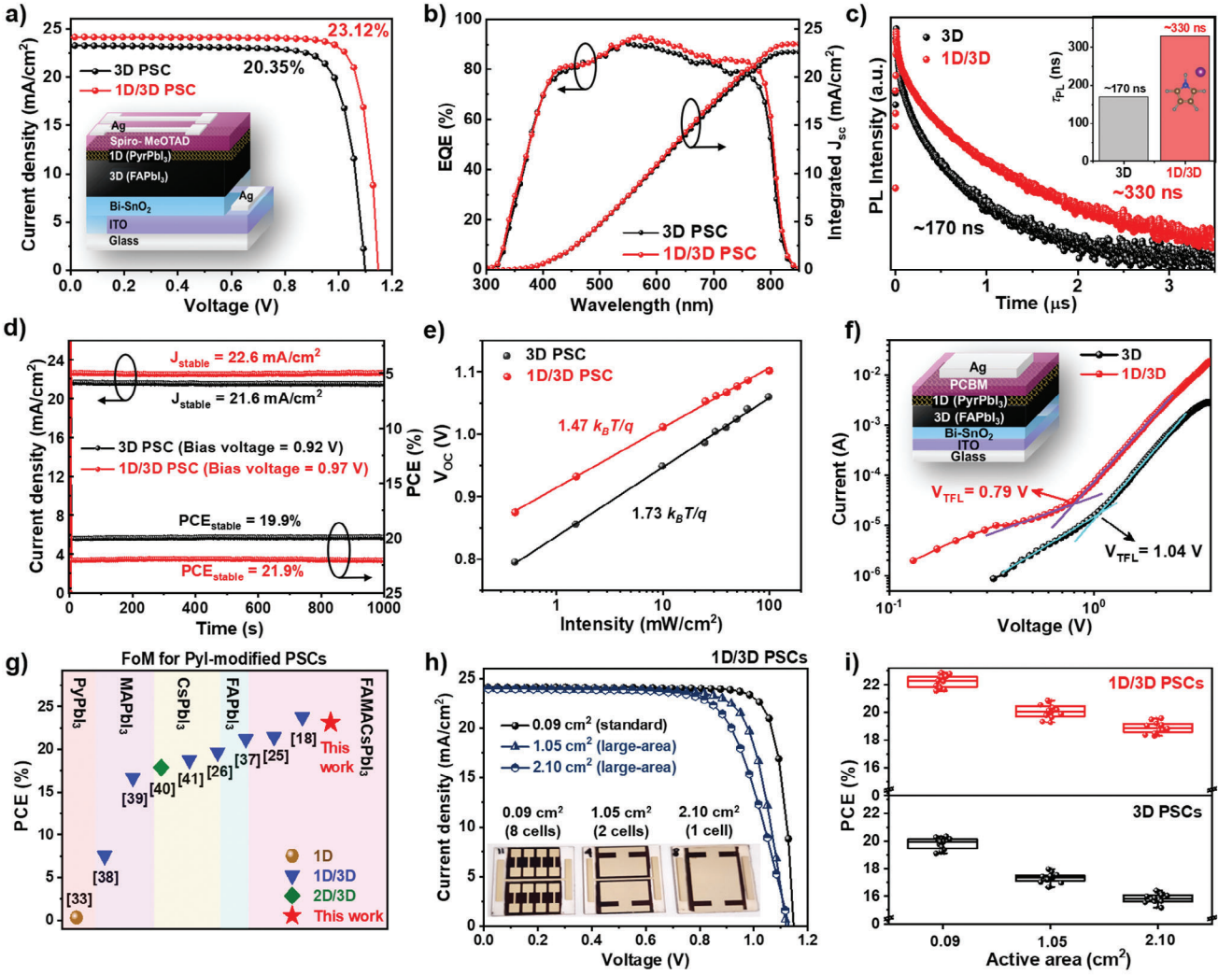

Figure 4. Device performance of PSCs: a) *J–V* characteristic curves and device architecture (inset), b) EQE and integrated J_{sc} plots of the champion 3D PSCs and 1D/3D PSCs. c) TRPL spectra of 3D and 1D/3D perovskite films. d) Steady-state current density and efficiency spectra and e) V_{oc} versus illumination intensity plots for 3D PSCs and 1D/3D PSCs. f) Dark *I–V* curves and device structure (inset) of 3D and 1D/3D single-carrier devices. g) Figure-of-Merits (FoM) plots of multi-dimensional (1D, 1D/3D and 2D/3D) PSC devices based on different PyI-modified perovskite films.[18,25,26,33,37–41] h) *J–V* curves of 1D/3D PSCs fabricated with different active areas. i) PCE distributions (whisker plots) of 3D PSCs and 1D/3D PSCs with the increase of active areas.

a compact-porous morphology and distinctive amorphous-crystalline charge transfer properties.[35] These properties are crucial for improving the ohmic contact and interfacial morphology between the ETL and the perovskite film, which is necessary for the scalable fabrication of PSCs. The current density-voltage (J-V) curves in Figure 4a show that the 3D PSC (pristine) device achieved a V_{oc} of 1.098 V, a J_{sc} of 23.31 mA cm^{-2}, and a fill factor (FF) of 79.52%, resulting in a PCE of 20.35%. A remarkable improvement was observed in all photovoltaic parameters of the PSC after PyI passivation, especially the V_{oc}. The PCE of the 1D/3D PSC device (target) device was improved to 23.12%, which was substantiated by an elevated V_{oc} of ≈1.149 V, a J_{sc} of 24.13 mA cm^{-2}, and an increased FF of ≈83.46%. Both 3D PSC and 1D/3D PSC exhibited a negligible hysteresis (Figure S11, Supporting Information). The 1D/3D PSC also exhibited a higher EQE than the 3D PSC in the UV–vis region (Figure 4b). From the EQE spectra, the integrated J_{sc} values for the 3D and 1D/3D PSCs were found to be 22.78 and 23.46 mA cm^{-2}, respectively, which correlates well with the measured J_{sc} values. In addition, the PCE histogram plots in Figure S12 (Supporting Information) show that the photovoltaic performance of the 1D/3D PSCs was consistently higher than the 3D PSCs.

To determine if the newly-formed 1D $PyPbI_3$ contributes to the photovoltaic performance of the 1D/3D PSCs, we fabricated 1D PSCs by replacing the 3D triple-cation perovskite absorber with 1D $PyPbI_3$. As shown in Figure S13 (Supporting Information), the PCE of the 1D PSC is rather low (<1%) because the 1D $PyPbI_3$ perovskitoids are known to exhibit a wide E_g and unidirectional charge transport, similar to the previous result reported by Xu's group.[33] Therefore, the PCE improvement of the 1D/3D PSCs observed herein can be primarily ascribed to the suppression of non-radiative recombination loss associated with defect

trap states in the 3D perovskite film following PyI modification. To validate our claim, we performed TRPL measurements to analyze the recombination dynamic of photoexcited charge carriers of both 3D and 1D/3D perovskite films. In the absence of ETL/HTL, the charge carriers generated in a perovskite film can either undergo band-to-band recombination to produce radiative emission or recombine non-radiatively in the shallow trap states.[34] The spectra data presented in Figure 4c reveals that the 1D/3D perovskite film exhibited a significantly slower fluorescence decay compared to its 3D counterpart. By employing a quadruple-exponential decay function (Equation S4), the fluorescence lifetime (τ_{PL}) of the perovskite film was determined to have increased from 170 ns (3D perovskite) to 330 ns (1D/3D perovskite) following PyI modification. Detailed fitting parameters for the calculations of τ_{PL} can be found in Table S5 (Supporting Information). The observed slower photoluminescence decay and extended τ_{PL} value imply a reduced non-radiative recombination rate in the 1D/3D perovskite film due to a lower presence of defect-induced trap states.

The operational stability test involved continuously recording the stabilized steady-state current density (J_{stable}) and PCE (PCE_{stable}) of the 3D PSCs and 1D/3D PSCs (tracked at the maximum power point, MPP) under one-sun illumination for 1000 s. Remarkably, neither device exhibited any noticeable decline in performance after the measurements (Figure 4d). However, the PCE_{stable} of the 1D/3D PSC (≈21.9%) was ≈10% higher than that of the 3D PSCs (~19.9%). Furthermore, the V_{oc} variations of the PSCs was investigated under different intensities. It was observed that the V_{oc} for both 3D and 1D/3D PSCs increased linearly with light intensity (Figure 4e), indicating that the presence of the 1D $PyPbI_3$ capping layer did not create an additional charge transport barrier in the PSCs. To gain insight into the recombination dynamics., the diode ideality factor (IF) of both 3D and 1D/3D PSCs was determined from their respective fitted k_BT/q slopes, where k_B represents the Boltzmann constant, T represents the temperature, and q represents the electric charge. Typically, a minor deviation in k_BT/q slope with IF = 1 reflects a dominant second-order bimolecular recombination, while a major deviation in k_BT/q slope with IF = 2 implies a dominant monomolecular Shockley–Read–Hall (SRH) recombination.[36] In view that the k_BT/q slope of 1D/3D PSC exhibited a smaller IF (1.47 k_BT/q) than the 3D PScs (1.73 k_BT/q), clearly demonstrating that the 1D $PyPbI_3$ capping layer helped to suppress trap-assisted SRH recombination in the PSCs through surface defects and grain boundary passivation.

For in-depth defect density analysis, space-charge-limited current measurements were performed on electron-only devices with a configuration of ITO/Bi-SnO_2/perovskite/PCBM/Ag, encompassing either 3D perovskite or 1D/3D perovskite films as photoabsorber. The trap-filled limited voltage (V_{TFL}) values of the single-carrier devices were fitted from the dark I–V curves (Figure 4f), and the trap density (N_{trap}) values were determined via Mott-Gurney relation (Equation S5, Supporting Information). The 1D/3D single-carrier device had a lower V_{TFL} of ≈0.79 V compared to the 3D counterpart with a V_{TFL} of ~1.04 V. Correspondingly, the trap densities of 1D/3D single-carrier device (7.23×10^{15} cm^{-3}) was lower than that of the 3D counterpart (9.82×10^{15} cm^{-3}). The reduced defects of 1D/3D perovskite film can help to suppress bimolecular carrier recombination, allowing 1D/3D PSC device to achieve tremendously higher PCE. As a comparison, Figure 4g and Table S6 (Supporting Information) summarize the photovoltaic performances of representative PSC devices based on PyI-modified perovskites with different compositions and dimensionalities (1D, 2D, 3D) that are available in the recent literature.[18,25,26,33,37–41] Among all studies, the 1D/3D (PyI-modified) PSC developed herein exhibited the highest PCE, manifesting the efficacy of PyI treatment strategy in the development of low-cost, high-performance perovskite absorber.

Furthermore, the long-term stability of 3D PSCs and 1D/3D PSCs under ambient air and in an inert environment (N_2-filled glovebox) was investigated. For stability tests, the Ag top contact in the PSCs was replaced with the extremely air-stable Au top contact (≈90 nm thick), and the devices were not encapsulated. After ≈2400 h of aging in an ambient environment (temperature: 18–23 °C; relative humidity: 15–20%), the PCE retention of the 3D PSCs deteriorated to well below 70%, whereas the PCE retention of 1D/3D PSCs remained above 85% under similar test conditions (refer to Figure S14a, Supporting Information). When stored in an N_2-filled glovebox (O_2 ppm <0.1; H_2O ppm < 0.1), the PCE deterioration of both 3D PSCs and 1D/3D PSCs was mitigated, with both devices exhibiting >80% PCE retention due to the lack of moisture and oxygen-induced degradations (Figure S14b, Supporting Information). The results demonstrated the superior stability of 1D/3D PSCs compared to the pristine PSCs, which is credited to the 1D $PyPbI_3$ capping layer that hindered the oxygen and moisture permeation into the perovskite film.

The scalability of the PSCs also benefited from the defect passivation effect of PyI, in addition to enhanced device performance and stability. For the scalability study, 3D PSCs and 1D/3D PSCs were fabricated with various active areas (0.09, 1.05, and 2.10 cm^2). Figure S15 (Supporting Information) shows that the PCE of 3D PSCs deteriorated rapidly from 20.35% (0.09 cm^2) to 17.44% (1.05 cm^2) and ≈15.51% (2.10 cm^2) as the active area increased. Large-area (>1 cm^2) PSCs typically exhibit lower PCE than their small-area (0.09 cm^2) counterparts due to increased series resistance and surface pinholes/defects that hinder lateral charge transport. However, in the case of 1D/3D PSCs, the PCE loss due to defects and inhomogeneities was mitigated through PyI passivation during scaling up. The top-performing large-area 1D/3D PSCs achieved a PCE of 20.72% and 18.99% for active areas of 1.05 and 2.10 cm^2, respectively (Figure 4h). The performance loss associated with the scale-up process for 3D PSCs and 1D/3D PSCs is compared in Table S7 (Supporting Information), in which the latter exhibited a higher PCE retention (≈82%) than the former (≈76%) with the increase of active area from 0.09 cm^2 to 2.10 cm^2. The performances of large-area 3D PSCs and 1D/3D PSCs were also highly consistent and reproducible, as shown by the PCE distribution analysis in Figure 4i. Taking average from 15 devices fabricated in four different batches, the large-area (2.10 cm^2) 3D PSCs and 1D/3D PSCs recorded an average PCE of ≈14.8% and ≈18.1% respectively, showing the increasingly higher PCE disparity between the two types of PSCs with the increase of active area.

For practical applications, perovskite modules are preferred over individual cells because they can generate significantly higher power output. Drawing inspiration from the more balanced performance-scalability tradeoff of the 1D/3D PSCs, we applied the PyI modification to fabricate perovskite solar

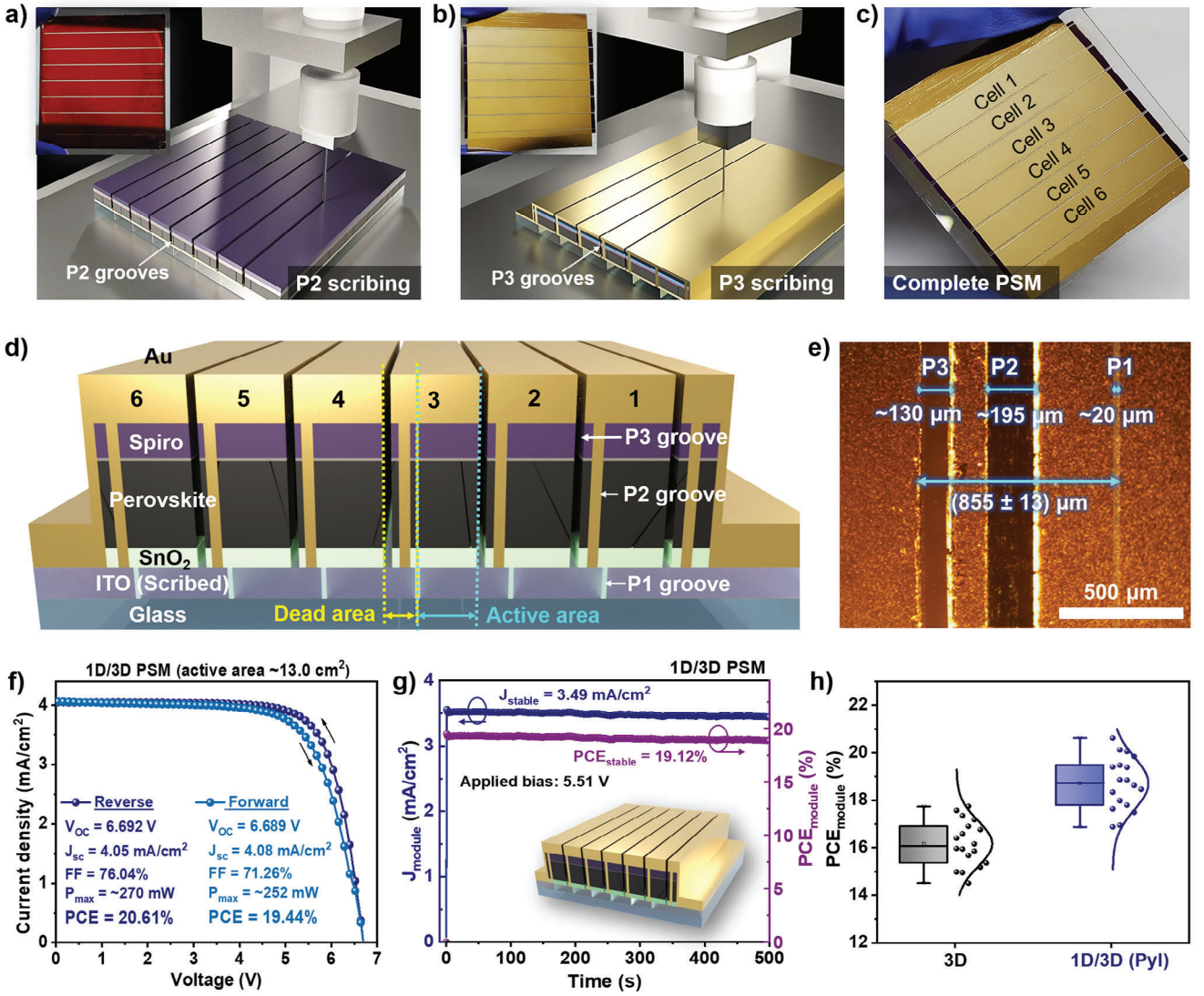

Figure 5. a) Schematic illustration of the low-cost mechanical scribing process of PSM performed using a 3D-DIW instrument. b) Digital image of a large-area perovskite film deposited on P1-scribed ITO substrate (left), large-area perovskite film after P2 scribing (center), and the complete PSM after P3 scribing (right). Schematic images showing the c) six series-connected cells and d) P1-P2-P3 electrical interconnections between the adjacent cells in the mechanically-scribed PSM. e) Optical microscopic image showing the P1, P2, P3 grooves and dead areas on the PSC. f) *J–V* curves and g) steady-state current density and PCE spectra of the top-performing 1D/3D PSC module tracked at MPP. h) Whisker plots showing the PCE distributions of 3D and 1D/3D PSMs.

minimodules (PSMs). The PSM is based on a device architecture similar to that of the 1D/3D PSCs except for the top contact and uses a P1-P2-P3 electrical interconnection scheme. However, the perovskite absorber film in the PSM was prepared using a vacuum-assisted drying technique instead of the antisolvent technique, as the latter is not effective in producing a uniform perovskite film over a large area. In order to lower the fabrication costs, the electrical interconnections in the PSMs were created using a mechanical scribing method with a 3D direct-ink writing (3D-DIW) instrument instead of laser scribing. The step-by-step fabrication process of the PSM, including the mechanical scribing part, is depicted in Figure S16 (Supporting Information). To summarize, the module fabrication process involved preparing a large-area 1D/3D perovskite absorber film and other functional layers (Bi-SnO_2 ETL and Spiro-MeOTAD HTL) on the P1-scribed (5 cm × 5 cm) ITO substrates (Figure S17, Supporting Information). Before gold (Au) contact deposition, the stacked functional layers (Bi-SnO_2/perovskite/Spiro-MeOTAD) were mechanically scribed off the ITO substrate with a metal needle at a moving speed of 2 mm s^{-1} to create P2 grooves (**Figure** 5a). After Au deposition, the module was mechanically scribed again to create P3 grooves that isolate the top Au contact to complete PSM fabrication (Figure 5b). The resulting PSM consisted of six subcells connected in series that collectively yielded a total active area of 12.0–14.0 cm^2 (Figure 5c). The schematic P1-P2-P3 interconnection architecture of these subcells is illustrated in Figure 5d.

Specifically, the P1 scribing process creates grooves in the bottom ITO electrode of neighboring cells for electrical isolation. The P2 scribing process selectively removes a slice of stacked functional layers on top of the glass/ITO substrate to create a series connection between the adjacent cells following the deposition of Au electrode. The P3 scribing process separates the top Au electrode for electrical isolation among the neighboring cells.[42] The spaces between the P1 and P3 grooves of the adjacent subcells are considered dead (photo-inactive) areas that do not contribute to photocurrent generation. The optical microscope image in Figure 5e visualizes the P1, P2, and P3 grooves on the champion 1D/3D PSM. By measuring the inter-distances and line widths of P1, P2, and P3 grooves, the champion 1D/3D PSM was found to have a geometrical fill factor (photoactive area/total area) as high as ≈87% with an active area of ≈13.0 cm^2. On the back of a high V_{OC} of 6.69 V, J_{SC} of 4.05 mA cm^{-2}, and FF of 76%, the best 1D/3D PSC module (≈13.0 cm^2) yielded an unprecedentedly high module efficiency (PCE_{module}) of 20.6% and a power output of ≈270 mW (Figure 5f). To the best of our knowledge, this is currently the highest performance achieved by mechanically-scribed PSMs. In a standard operational reliability test, the 1D/3D PSM recorded less than a 2% drop in PCE after 500 s of continuous maximum power point tracking under one-sun illumination, yielding a J_{stable} of 3.49 mA cm^{-2} and a PCE_{stable} of 19.1% (Figure 5g). The 1D/3D PSMs also exhibited consistently higher PCE_{module} than the pristine 3D PSMs throughout different batches of fabrication (Figure 5h), which we attribute to improved homogeneity and reduced morphological defects of the 1D/3D perovskite film. The excellent photovoltaic performance of the 1D/3D PSMs achieved herein demonstrated the scalability of 1D/3D perovskite absorber film, on top of highlighting the compatibility of mechanical scribing technique with the low-cost production of perovskite photovoltaics.

3. Conclusion

In summary, we have demonstrated the use of a bulky organic passivator, namely PyI, to fine-tune the dimensionality and structural stability of $FAPbI_3$ perovskite film, which notably enhanced the efficiency and stability in PSCs. Our innovative passivation strategy has led to the formation of a 1D $PyPbI_3$ capping layer atop the 3D $FAPbI_3$ perovskite absorber film, effectively reducing the surface defects and grain boundaries that cause non-radiative recombination of charge carriers. Structural characterizations reveal that the $PyPbI_3$ perovskitoids can create a lattice-matched 1D–3D interface through bonding interactions with the uncoordinated Pb ions/atoms on the surface of $FAPbI_3$ perovskite. After PyI passivation, the newly formed 1D/3D perovskite film exhibited an extended fluorescence lifetime due to the reduction of deep trap states associated with defects. As a result, the 1D/3D PSC device achieved a remarkable PCE of ≈23.1%, outperforming the pristine 3D PSC device (PCE of ≈20.3%). Furthermore, the 1D/3D PSCs displayed superior scalability and stability due to the bifunctional role of the 1D capping layer as a defect passivator and degradation barrier. The improved scalability of 1D/3D PSCs enabled the mechanically scribed PSC module (active area ≈13.0 cm^2) to produce a PCE_{module} of ≈20.6% with a total power output of ≈270 mW. The use of PyI for dimensionality engineering is cost-effective and easily reproducible. Notably, this work highlights the benefits of utilizing multi-dimensional (1D/3D) perovskite structures and mechanical scribing for the fabrication of low-cost PSC devices with competitive performance at both the cell and module levels.

4. Experimental Section

Fabrication of PSC Devices and Modules: Conventional *n-i-p* structured PSC devices were fabricated using a solution-based method, employing a amorphous–crystalline Bi-SnO_2 as electron transport layer (ETL) and spiro-MeOTAD as hole transport layer (HTL).[35] To fabricate 3D perovskite film, a 1.8 M of $FAPbI_3$-based triple-cation perovskite precursor solution was prepared using pre-synthesized δ-$FAPbI_3$ crystallite powder and methylammonium chloride (MACl), and doped with 7.5 vol.% of CsI-PbI_2 complex additive (1.15 M in DMSO).[3] The perovskite films were prepared on ITO substrates using a one-step antisolvent technique, employing ethyl acetate-hexane (7:3 vol/vol) as mixed antisolvent. To fabricate 1D/3D multi-dimensional perovskite film, 100 µL of PyI solution (0.5–5.0 mg mL^{-1} in IPA) was spin-casted onto the as-prepared perovskite film at 5000 rpm for 40 s in an N_2 glovebox and left for overnight drying. Then, spiro-MeOTAD HTL and Ag top contacts were spin-coated and thermally evaporated, respectively, onto the perovskite films to complete the device fabrication process. For the fabrication of PSM, large-area perovskite film was prepared on readily P1-scribed ITO substrates (5 cm × 5 cm) using a vacuum-assisted drying technique. Mechanical scribing processes of PSMs were performed using a 3D-DIW instrument (SHOTMASTER 350Ωx, Musashi Engineering, Japan). The top Ag contacts were replaced with Au contacts for the fabrication of PSM. The detailed fabrication recipes of the PSCs and PSMs are provided in Section S1.2 (Supporting Information) and Section S1.3 (Supporting Information), respectively. Additionally, the step-by-step fabrication process of the PSM, including the mechanical scribing part, can be found in Figure S16 (Supporting Information).

Materials and Device Characterizations: The surface morphologies and crystallographic changes of the perovskite films were examined using a field-emission scanning electron microscope (FESEM, SUPRA40VP, Carl Zeiss, Germany) and an X-ray diffractometer (XRD, X'PERT-PRO, PANalytical), respectively. The lattice fringes of the perovskite films were visualized using a Cs-corrected high-angle annular dark-field scanning transmission electron microscopy (HAADF-STEM, JEM-ARM 200F, JEOL, Korea). All of the characterization facilities mentioned are installed at the Center for University-wide Research Facilities (CURF) at Jeonbuk National University. The optical absorption and photoluminescence of the perovskite films were measured by a UV–vis spectrometer (PerkinElmer Lambda 750, USA) and a fluorescence spectrophotometer (FluroMax-4, Horiba, Japan), respectively. The surface composition and work function of the perovskite films were analyzed using an X-ray photoelectron spectroscopy (XPS, Multi Lab 2000, Thermo Scientific, USA). The ATR-FTIR spectra of the perovskite films were collected from a Fourier transform infrared spectrometer (FTIR, Spectrum 3, Perkin Elmer, USA) using an attenuated total reflectance method. The vertical composition and depth-dependent positive/negative ion distributions (depth profiles) of the perovskite films were acquired from a time-of-flight secondary-ion mass spectrometry (ToF-SIMS 5, ION-TOF, Germany). Time-resolved PL (TRPL) profiles of the perovskite films were acquired from a time-correlated single-photon counting system (TC-SPC, TimeHarp 260, PicoQuant, Germany). The current density–voltage (*J–V*) curves of the PSCs and PSMs were measured by a source-measure-unit instrument (Keithley 2400, Tektronix, USA) under 1-sun illumination by a solar simulator (Oriel 3A, Newport, USA) equipped with an AM 1.5G filter. The EQE of the PSCs was measured using a quantum efficiency measurement system (Oriel IQE-200, Newport, USA). The performances of the PSC devices were measured in ambient air without any preconditioning. The detailed characterization information of the perovskite films and PSC devices is available in Supporting Information.

Statistical Analysis: The PCE values of PSCs (n = 15) and PSMs (n = 18) were statistically analyzed in the form of Whisker plots using Origin 9.0 software, as shown in Figures 4i and 5h, respectively.

Additionally, Origin 9.0 software was used to generate Whisker plots (n = 25) for the photovoltaic parameters (V_{oc}, J_{sc}, FF, and PCE) of PSCs in Figure S12 (Supporting Information). The grain size distributions of perovskite films were represented through histogram plots (n = 50) in Figure S2 (Supporting Information), which were based on the measurement values obtained from ImageJ software.

Supporting Information

Supporting Information is available from the Wiley Online Library or from the author.

Acknowledgements

This work was financially supported by the Basic Science Research Program (NRF-2021R1A2C2004206) through the National Research Foundation (NRF) of Korea, funded by the Ministry of Science, ICT & Future Planning. This work was supported by the Korea Electric Power Corporation (CX72220014). This work was supported by the selection of a research-oriented professor at Jeonbuk National University in 2024.

Conflict of Interest

The authors declare no conflict of interest.

Author Contributions

H.B.L. and A.M. contributed equally to this work. H.B.L. conceptualized the idea for the study; visualized the study; wrote the original draft; designed the methodology; and performed experimental work, formal analysis, and investigation. A.M. performed experimental work, wrote, reviewed, and edited the manuscript; and performed formal analysis and data curation. N.K. performed formal analysis; wrote, reviewed, and edited the manuscript; and performed data curation. N.H.Z.K. performed experimental work and data curation. V.V.S. performed formal analysis and wrote, reviewed, and edited the manuscript. B.T. designed the methodology and performed formal analysis. D.-H.K. designed methodology. J.-W.K. performed supervision and project administration; wrote, reviewed, and edited the manuscript; and performed funding acquisition.

Data Availability Statement

The data that support the findings of this study are available in the supplementary material of this article.

Keywords

defects, dimensionality engineering, grain boundaries, passivation, perovskitoids

Received: June 6, 2024
Revised: July 31, 2024
Published online:

[1] J. Park, J. Kim, H. S. Yun, M. J. Paik, E. Noh, H. J. Mun, M. G. Kim, T. J. Shin, S. Il Seok, *Nature* **2023**, *616*, 724.
[2] T. Niu, L. Chao, X. Dong, L. Fu, Y. Chen, *J. Phys. Chem. Lett.* **2022**, *13*, 1845.
[3] H. B. Lee, R. Sahani, V. Devaraj, N. Kumar, B. Tyagi, J. Oh, J.-W. Kang, *Adv. Mater. Interfaces* **2023**, *10*, 2201658.
[4] J.-W. Lee, S. Tan, S. Il Seok, Y. Yang, N.-G. Park, *Science* **2022**, *375*, eabj1186.
[5] Y. Wang, D. Zheng, K. Wang, Q. Yang, J. Qian, J. Zhou, S. (Frank) Liu, D. Yang, *Angew. Chem., Int. Ed.* **2024**, *63*, 202405878.
[6] J. Hidalgo, W. Kaiser, Y. An, R. Li, Z. Oh, A.-F. Castro-Méndez, D. K. LaFollette, S. Kim, B. Lai, J. Breternitz, S. Schorr, C. A. R. Perini, E. Mosconi, F. De Angelis, J.-P. Correa-Baena, *J. Am. Chem. Soc.* **2023**, *145*, 24549.
[7] P. Shi, Y. Ding, B. Ding, Q. Xing, T. Kodalle, C. M. Sutter-Fella, I. Yavuz, C. Yao, W. Fan, J. Xu, Y. Tian, D. Gu, K. Zhao, S. Tan, X. Zhang, L. Yao, P. J. Dyson, J. L. Slack, D. Yang, J. Xue, M. K. Nazeeruddin, Y. Yang, R. Wang, *Nature* **2023**, *620*, 323.
[8] Q. Li, S. Gaastra-Nedea, D. Smeulders, S. Tao, *EcoMat* **2023**, *5*, e12320.
[9] H. B. Lee, M. Jeon, N. Kumar, B. Tyagi, J.-W. Kang, *Adv. Funct. Mater.* **2019**, *29*, 1903213.
[10] M. Kim, G. H. Kim, T. K. Lee, I. W. Choi, H. W. Choi, Y. Jo, Y. J. Yoon, J. W. Kim, J. Lee, D. Huh, H. Lee, S. K. Kwak, J. Y. Kim, D. S. Kim, *Joule* **2019**, *3*, 2179.
[11] F. Wang, S. Bai, W. Tress, A. Hagfeldt, F. Gao, *npj Flex. Electron.* **2018**, *2*, 22.
[12] S. Pandey, J. Ko, B. Park, J. Byun, M.-J. Lee, *Chem. Eng. J.* **2023**, *466*, 143019.
[13] M. Liu, T. Pauporté, *Nanomicro Lett.* **2023**, *15*, 134.
[14] H. B. Lee, N. Kumar, B. Tyagi, S. He, R. Sahani, J.-W. Kang, *Mater. Today Energy* **2021**, *21*, 100759.
[15] C. Zhu, X. Niu, Y. Fu, N. Li, C. Hu, Y. Chen, X. He, G. Na, P. Liu, H. Zai, Y. Ge, Y. Lu, X. Ke, Y. Bai, S. Yang, P. Chen, Y. Li, M. Sui, L. Zhang, H. Zhou, Q. Chen, *Nat. Commun.* **2019**, *10*, 815.
[16] R. Chakraborty, A. Nag, *Phys. Chem. Chem. Phys.* **2021**, *23*, 82.
[17] L. Yan, S. Qiu, B. Yu, J. Huang, J. Qiu, C. Zhang, F. Guo, Y. Yang, Y. Mai, *Adv. Energy Sustainability Res.* **2022**, *3*, 2100191.
[18] J. Cha, C. Beom Lee, S. Min Park, D. Baek, S. Kim, S. Gyo Han, H. Jin, S. Joo Yang, J. Lim, K. Kim, M. Kim, *Chem. Eng. J.* **2024**, *484*, 149280.
[19] X. Zhao, T. Liu, Y. L. Loo, *Adv. Mater.* **2022**, *34*, 2105849.
[20] Q. Chen, K. Deng, Y. Shen, L. Li, *InfoMat.* **2022**, *4*, e12303.
[21] Y. Meng, W. Zhang, X. Zhang, Y. Deng, H. Zhang, G. Zeng, G. Liu, X. Li, *ChemSusChem* **2023**, *16*, 202300257.
[22] S. Akin, N. Arora, S. M. Zakeeruddin, M. Grätzel, R. H. Friend, M. I. Dar, *Adv. Energy Mater.* **2020**, *10*, 1903090.
[23] J. Wang, L. Liu, S. Chen, L. Qi, M. Zhao, C. Zhao, J. Tang, X. Cai, F. Lu, T. Jiu, *Small* **2022**, *18*, 2104100.
[24] D. Duan, C. Ge, M. Z. Rahaman, C.-H. Lin, Y. Shi, H. Lin, H. Hu, T. Wu, *NPG Asia Mater.* **2023**, *15*, 8.
[25] Y. Du, J. Wu, X. Zhang, Q. Zhu, M. Zhang, X. Liu, Y. Zou, S. Wang, W. Sun, *J. Energy Chem.* **2021**, *52*, 84.
[26] A. F. Xu, N. Liu, F. Xie, T. Song, Y. Ma, P. Zhang, Y. Bai, Y. Li, Q. Chen, G. Xu, *Nano Lett.* **2020**, *20*, 3864.
[27] X. Zhou, X. Liang, F. Wang, H. Sun, Q. Zhu, H. Hu, *Chem. Eng. J.* **2024**, *493*, 152539.
[28] M.-Y. Hao, H.-Y. Wang, Y. Wang, Y. Qin, J.-P. Zhang, X.-C. Ai, *J. Power Sources* **2020**, *479*, 229077.
[29] M. Fu, X. Shan, S. Wang, X. Zhao, R. Tao, L. You, Z. Deng, X. Fang, G. Meng, *ACS Appl. Electron. Mater.* **2024**, *6*, 4876.
[30] J. D. McGettrick, K. Hooper, A. Pockett, J. Baker, J. Troughton, M. Carnie, T. Watson, *Mater. Lett.* **2019**, *251*, 98.
[31] B. G. H. M. Groeneveld, S. Adjokatse, O. Nazarenko, H.-H. Fang, G. R. Blake, G. Portale, H. Duim, G. H. ten Brink, M. V. Kovalenko, M. A. Loi, *Energy Technol.* **2020**, *8*, 1901041.
[32] S. Sidhik, Y. Wang, M. De Siena, R. Asadpour, A. J. Torma, T. Terlier, K. Ho, W. Li, A. B. Puthirath, X. Shuai, A. Agrawal, B. Traore, M. Jones, R. Giridharagopal, P. M. Ajayan, J. Strzalka, D. S. Ginger, C. Katan, M.

A. Alam, J. Even, M. G. Kanatzidis, A. D. Mohite, *Science* **2022**, *377*, 1425.
[33] F. Xu, Y. Li, N. Liu, Y. Han, M. Zou, T. Song, *Crystals* **2021**, *11*, 241.
[34] H. B. Lee, N. Kumar, S. Cho, S. Hong, H. H. Lee, H. J. Kim, J.-S. Lee, J.-W. Kang, *Adv. Energy Sustainability Res.* **2023**, *4*, 2200128.
[35] H. B. Lee, N. Kumar, M. M. Ovhal, Y. J. Kim, Y. M. Song, J.-W. Kang, *Adv. Funct. Mater.* **2020**, *30*, 2001559.
[36] Y. Luan, F. Wang, J. Zhuang, T. Lin, Y. Wei, N. Chen, Y. Zhang, F. Wang, P. Yu, L. Mao, H. Liu, J. Wang, *EcoMat.* **2021**, *3*, e12092.
[37] P. Liu, Y. Xian, W. Yuan, Y. Long, K. Liu, N. U. Rahman, W. Li, J. Fan, *Adv. Energy Mater.* **2020**, *10*, 1903654.
[38] M. K. Rao, M. Selvakumar, M. G. Mahesha, S. Paramasivam, R. Dileep K, N. S. Prabhu, G. Veerappan, S. Senthilkumar, S. D. Kamath, *Mater. Chem. Phys.* **2023**, *303*, 127668.
[39] N. D. Pham, Y. Yang, M. T. Hoang, T. Wang, V. T. Tiong, G. J. Wilson, H. Wang, *Energy Technol.* **2020**, *8*, 1900918.
[40] Q. Zhang, Y. Guo, H. Liu, W. Li, L. Zhu, H. Chen, *J. Renew. Mater.* **2023**, *11*, 3193.
[41] L. Zhang, T. Guo, B. Liu, D. Du, S. Xu, H. Zheng, L. Zhu, X. Pan, G. Liu, *ACS Appl. Mater. Interfaces* **2022**, *14*, 19614.
[42] F. Di Giacomo, L. A. Castriotta, F. U. Kosasih, D. Di Girolamo, C. Ducati, A. Di Carlo, *Micromachines* **2020**, *11*, 1127.